AFM characterization of physical properties in coal adsorbed with different cations induced by electric pulse fracturing

Qifeng Jia [a,b,c], Dameng Liu [a,b,*], Yidong Cai [a,b], Yingfang Zhou [c,d], Zheng Zhao [a,b], Yanqing Yang [e]

[a] *School of Energy Resources, China University of Geosciences, Beijing 100083, China*

[b] *Coal Reservoir Laboratory of National Engineering Research Center of CBM Development & Utilization, China University of Geosciences, Beijing 100083, China*

[c] *School of Engineering, Fraser Noble Building, King's College, University of Aberdeen, AB24 3UE Aberdeen, UK*

[d] *Department of Energy Resources, University of Stavanger, Stavanger, 4021, Norway*

[e] *Shanxi Lanyan Coalbed Methane Engineering Research Co., Ltd., Jincheng 048000, China*

* Corresponding author at: School of Energy Resources, China University of Geosciences, Beijing 100083, China.

E-mail address: dmliu@cugb.edu.cn (D. Liu), Tel: +86-10-82323971; fax: + 86-10-82326850.

Abstract

Pore system in coal is highly heterogeneous, while it is the main occurrence space and transport channel for coalbed methane (CBM). Electric pulse fracturing (EPF) has been considered as an effective approach to improve the coal physical properties for better CBM production. In this work, based on AFM measurement of 40 coal samples collected from Qinshui Basin, we evaluated the physical properties of coal, adsorbed with different cations, after EPF. This was accomplished by first analyzing the breakdown field response process of coal adsorbed with different cations, and then determining the dynamic changes of pore and surface roughness using the watershed

method. In the PeakForce QNM™ model, the heterogeneous distribution of the adhesion force with increasing cation valence was quantified. The results show that the ability of medium- and high-rank coals to adsorb cations exhibits in the order of Fe^{3+} > Ca^{2+} > K^{+}, attributed to the decrease in the radius of hydrated ions with increasing ionic valence. When the electric field is applied to both ends of coal sample, the plasma channels in coal generate huge energy, resulting in the temperature rise of pore-fracture and throat. Affected by EPF, the porosity of Chengzhuang (CZ) increases from 4.1% to 27.4%, greater than that of Qiyi (QY) from 6.7% to 14.5%. In the surface morphology tests, the surface skewness R_{sk} of QY adsorbed with different valence cations shifts from positive to negative values, reflecting the change of coal surface height from the right-skewed normal distribution to the left-skewed one. Moreover, the area where the surface height of QY adsorbed cation is below the average value gradually increases with the increase of the chemical valence. For micromechanical properties, the adhesion force of CZ adsorbed with different cations ranges from 0.9 to 20.7 nN, which is less than QY overall. This is mainly due to the weakening of intermolecular forces on the coal surface with the deepening of coalification, resulting in a decrease in adhesion force. Therefore, this study provides new insights into the differences in gas production mechanisms of CBM wells in the same coal seam from different regions.

Keywords: Coal; AFM; Cation; Electric pulse fracturing, Physical properties

1. Introduction

As an essential fossil resource, the green mining of coal has become a key theme for efficient energy utilization in the era of "carbon peaking and carbon neutrality" [1-

6]. Coal reservoir, containing special properties such as multi-scale pore-fractures, large specific surface area and fluid conduction medium, results in diverse production modes of coalbed methane (CBM) in different areas [7, 8]. The geological resources of CBM in China with a depth of 2000 m are 30×10^{12} m³ [9-11], among which the recoverable resources in favorable areas with realistic exploitable value are 4×10^{12} m³, mainly distributed in the southern Qinshui Basin, the eastern of Ordos Basin and the southern Junggar Basin [12, 13].

The material composition, microstructure, and fluid-solid interface characteristics of coal reservoirs differ significantly from conventional oil and gas reservoirs [14-16], leading to a more complex fluid transfer theory in coal. These are mainly reflected in: (i) the existence of a large number of micro-and nano-pore spaces in coal reservoirs, which adsorb nearly 90% of CBM, controlling the occurrence and output of CBM [17]; (ii) the expansion of pores at the edge of coal samples under the action of stress to form large pores and fracture structures, leading to the increase of porosity [18]; (iii) the existence of dynamic geological interactions between coal matrix and mixed multiphase fluids under pressure, stress and temperature environments [19]; (iv) the process of CBM production including the multi-stage mass transfer effect of desorption-diffusion-seepage [20]. Therefore, it is necessary to further clarify the physical characteristics of coal reservoirs to improve the recovery of CBM [21-24].

Coal, as a dual porous medium, consists of matrix pore and fracture system [25, 26]. Among them, matrix pore is the main storage space for methane, and fracture is the main seepage channel for fluid [6]. Affected by metamorphism, sedimentary

environment, tectonism and magmatic activity, the physicochemical properties of coal reservoirs in the same block vary. Generally, the higher the content of vitrinite and semifusinite, the larger the pore volume of coal [27]. In contrast, the heterogeneity of coal with high content of inertinite and mineral is stronger [27, 28]. The porosity of coal shows a "U" trend with vitrinite reflectance and a negative correlation with ash content [29]. The pore-fracture is closely related to the seepage effect, as shown by the increased permeability with the fracture surface density. When the direction of osmotic pressure is parallel to the fracture surface [30], the permeability of coal reaches the maximum. In short, many scholars believe that the physical differences in coal reservoirs are caused by the coupling effect of effective stress and fluid pressure during the evolution of different geological histories [30, 31].

Due to the multi-period, diversity and variability of coal-forming environments, coal reservoirs exhibit strong heterogeneity and anisotropy [32-34], which brings challenges to the accurate characterization of physical properties. Many testing techniques, including field emission scanning electron microscope (FS-SEM), high-pressure mercury injection, nuclear magnetic resonance (NMR), liquid nitrogen adsorption, CT scanning, and Atomic Force Microscope (AFM) [35-39], have been used to evaluate the properties of coal. Kutchko et al. [40] found by FS-SEM that the size and number of pores did not change in supercritical CO_2 and that this dried CO_2 did not affect the coal properties as much as organic solvents. Zhang et al. [41] used high-pressure mercury injection to characterize low-, medium-, and high-rank coals, concluding that the pore structure of coal displayed multiple fractal characteristics

strongly influenced by the degree of coalification. As the content of the inertinite increases, the complexity of the pore structure of coal decreases due to the reduced heterogeneity in the low-value region of the pore volume. To capture the relaxation and diffusion behavior of fluids in coal seams, O'Neill et al. [42] proposed an NMR technique to determine the in-situ adsorbed gas concentrations within coal seams. This technique optimized the echo diffusion editing pulse train to calculate the concentrations of different gases in the coal reservoir using a two-dimensional inversion algorithm. Through liquid nitrogen adsorption experiments, Zhang et al. [43] discovered that plasma action during electric pulse fracturing (EPF) would increase the total volume and area of micropores, leading to an increase in coal desorption of 50% to 70%. Zhao et al. [44] investigated the effect of nano-pore structure on coal strength using CT scanning, concluding that coal particle strength decreases with increasing porosity. Also, the coal particle strength anisotropy was logarithmically related to the anisotropy of the pore structure. Lu et al. [45] obtained the influence of wettability on the surface properties of coal by AFM, and believed that the contact angle was negatively correlated with roughness because of the different adsorption sites of coal particles on water molecules. Recent studies have found that the distribution of elastic modulus on the microscopic surface of coal shows non-uniformity and an increase in local elastic modulus as the load intensity increases [46, 47]. Besides, Tian et al. [48] divided coal and gas outburst into four stages and proposed the concept of critical velocity of gas adsorption. Only gas molecules moving at a velocity smaller than the critical velocity for gas adsorption can adsorb to the coal surface, which provides new

evidence for understanding the microscopic mechanisms of gas fugacity, transport and protrusion in coal seams [49]. It can be seen from the literature that the physical characteristics and characterization techniques of coal reservoirs have been studied more extensively. However, there are few studies on the electric field distribution, surface roughness changes and micromechanical properties of coal adsorbed with different cations during EPF by AFM.

In this paper, the characteristics of physical property changes of coal adsorbed with different cations in the process of EPF were investigated by AFM tests; these were accomplished by first analyzing the process of medium- and high-rank coals adsorbed with different cations, and then determining the voltage, electric field and energy change of coals during EPF process. Subsequently, the physical property changes of coal were quantified by combining FE-SEM and AFM testing techniques. To evaluate the micromechanical properties of coal, the distribution characteristics of adhesion with the degree of coalification after EPF were characterized. This research provides new insights into the differences in gas production mechanisms of CBM wells in the same coal seam from different regions.

2. Sample and experimental systems

2.1. Sample preparation

Samples collected from the Chengzhuang (CZ) and Qiyi (QY) coal mines in the Qinshui Basin were employed to test the base parameters (Fig. 1). The collected samples are typically representative because the CBM wells around each of the two

coal mines exhibit similar drainage characteristics. According to the national standards GB/T 6948-1998 and GB/T 212-2008 [16, 50], the maximum vitrinite reflectance ($R_{o,max}$) and industrial components were determined by Leitz MPV-III microphotometer and automatic industrial analyzer SDLA618, respectively. Subsequently, a vertical drilling machine was used to drill 40 coal columns with dimensions of Φ 50×25 mm, followed by drying coal samples in a drying oven at 100°C. This eliminates the effect of moisture on the EPF experiment [51], reducing the experimental results' error. As shown in Table 1, CZ exhibits a maximum vitrinite reflectance of 2.92, indicating that the high-rank coal experienced a strong magmatic thermal metamorphism [52-54]. In contrast, QY was tested with a maximum vitrinite reflectance of 1.79, reflecting a lower degree of magmatic intrusion than CZ. Thus, CZ and QY belong to high- and medium-rank coals, respectively. The mineral filling can be observed on the surface of the former, while partial fractures can be seen on the latter. The coal maceral composition tests show that CZ displays vitrinite of 90.9% and no exinite. Regardless of CZ or QY, the vitrinite content is relatively lower in the region closer to magma contact. Additionally, both coal samples exhibit the highest fixed carbon content and the lowest moisture content in the industrial analysis. The ash content of CZ is greater than the volatile matter content, while the opposite is true for QY. This is because the degree of devolatilization and oxidation effects of coal samples increases with coalification.

Table 1 Sample information and basic parameters of the selected coals.

Samples	$R_{o,max}$	Per	Proximate analysis (%)				Coal maceral composition (%)	
	(%)	(mD)	M_{ad}	A_{ad}	V_{ad}	FC_{ad}	V	I
CZ	2.92	0.03	0.55	18.15	6.42	74.88	90.9	9.1
QY	1.79	0.07	1.33	9.86	13.63	75.18	92.6	7.4

Note: Per, permeability; M_{ad}, moisture (air-dried basis); A_{ad}, ash (dry basis); V_{ad}, volatile matter (dry, ash-free basis); FC_{ad}, Fixed carbon (air-dried basis); V, vitrinite; I, inertinite; E, exinite.

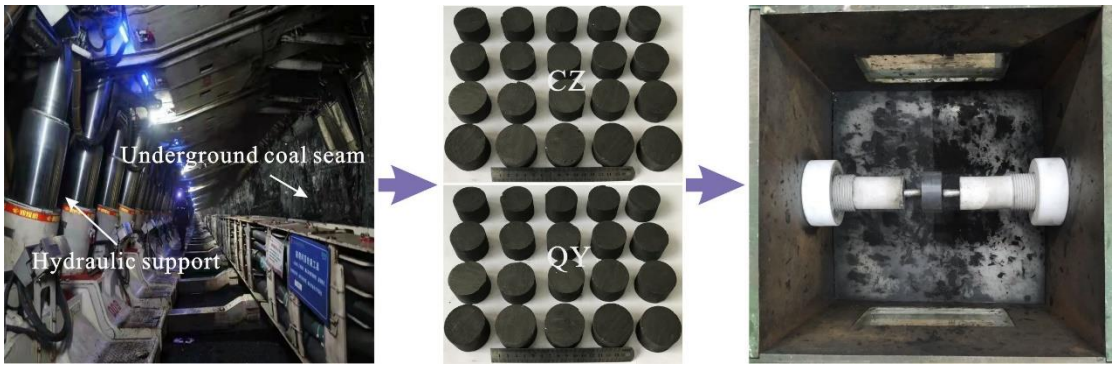

Fig. 1. Prepared medium- and high-rank coal columns.

2.2. EPF and AFM

The experimental system mainly contains EPF coal body and AFM testing (Fig. 2). The EPF device, from the Key Laboratory of Gas and Fire Control for Coal Mines, China University of Mining and Technology, is equipped with a capacitor, transformer, resistor, discharge switch, sample chamber, and digital oscillograph (Fig. 2b). The whole device allows a maximum output voltage of 50kV and can freely convert the AC to DC voltage through the transformer. To prevent damage to the instrument caused by the sudden discharge of the discharge switch closure, a 10KΩ resistor is connected between the transformer and the capacitor. The capacitor with a range of 0 to 8 μF can release the energy of 0-10 KJ, thus ensuring that coal sample can be cracked. During the entire electric pulse fracturing process, the direct contact between the discharge electrode and the solid material causes the generation of plasma channels inside coal sample, resulting in the focusing of energy inside the coal body to 100-1000 J/mm in a very short time. At the same time, great expansion stress is formed inside the coal body,

followed by the tensile damage of coal sample [55]. The superposition of electrical energy and swelling stress leads to a great shock wave inside coal sample, which makes coal sample break [56].

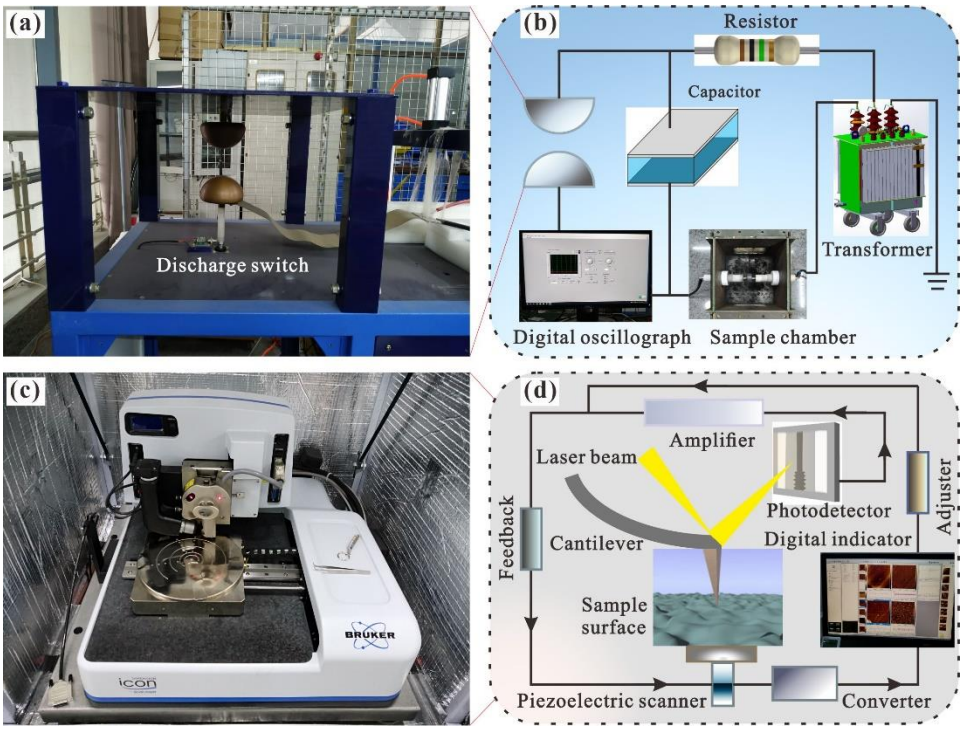

Fig. 2. Experimental system of EPF and AFM. (b) shows the schematic diagram of EPF (a), and (d) is the scanning schematic of AFM (c). In PeakForce QNM^{TM} mode, the section information in Fig. 3b and c can be obtained by scanning the probe in contact with the selected coal sample area in Fig. 3a.

The AFM device, model Dimension, from the State Key Laboratory of Tribology Tsinghua University, mainly includes laser beam, cantilever, photodetector, piezoelectric scanner, amplifier, converter, and adjuster (Fig. 2d). AFM is popular for characterizing the surface morphology and micromechanical properties of solids because of the ability to visualize the interaction between probe and coal surface [14, 15]. According to the physical properties of coal, the PeakForce QNM^{TM} mode is

selected to lightly touch the surface of coal sample (10×10×5 mm) so that the coal body can produce resonance with the cantilever beam. The entire device contains anti-vibration equipment and provides a scanning range of 90 × 90 × 10 μm in the X, Y and Z directions. In AFM measurements, we choose probes in tap mode, made of silicon wafers or silicon nitride. The longitudinal resolution is 0.03 nm, and the lateral resolution is 0.2 nm. Additionally, the thermal drift level is less than 0.2 nm/min.

2.3. Experimental procedures

The whole experimental procedure was divided into sample treatment, EPF and AFM tests (two tests before and after fracturing). During the sample treatment, 40 coal samples were placed in a vacuum drying chamber at 100°C for 24h, and the quality of coal samples was recorded. Then, coal samples were immersed in 0.2, 0.4, 0.6, 0.8, 1.0, 1.2 mol/L KCl, $CaCl_2$ and $FeCl_3$ solutions for 48h, during which the weight was measured every 4 hours. When the weight difference of the same coal sample for three consecutive times was less than 0.1 g, the adsorption saturation state was considered. The EPF stage was divided into three steps: (i) fixing the prepared coal column in the sample chamber and connecting it to the high-voltage electrode; (ii) closing the discharge switch to charge the capacitor with a step length of 0.3kV until coal sample was broken; (iii) recording the changes of voltage and current during the whole fracturing process by a digital oscillograph. Subsequently, the surface morphology and micromechanical properties of the eight coal samples were tested by AFM. After selecting the tap mode, we moved the probe close to sample to observe the surface morphology of coal by adjusting the laser. Meanwhile, the overlap of Trace and Retrace

curves in the Height Sensor plot was observed. It should be noted that coal samples were polished immediately after the initial drying, followed by the first AFM test; coal samples were polished again for the second AFM test after the completion of EPF. During the AFM measurements, the probe resonates under the external force, and part of the vibration position belongs to the repulsion region of the force curve. Due to the interstitial contact of the probe with sample surface, the phenomenon of coal powder adhesion should be avoided as much as possible. The low probe-sample interaction force in tap mode is particularly beneficial for improving resolution. Also, the lifetime of the probe is slightly longer than that of the contact mode.

3. Methodology

3.1. Cation adsorption and electric field variations

Since coal surface generally carries a negative charge, cation adsorption occurs in addition to wetting, hydration and dissolution when coal comes in contact with salt solutions [55]. Normally, coal is weak or non-conducting in conductivity. When coal is in contact with electrolyte solution, the conductive ions enter the pore from coal matrix, thus affecting EPF effect. By comparing the concentration difference in different cationic solutions, the adsorption capacity Γ of medium- and high-rank coals to cationic solutions can be obtained [51].

$$\Gamma = \frac{(C_i - C_e - \Delta C)V_i M}{1000 m_0} \qquad (1)$$

where C_i and C_e represent the initial concentration of the cation solution and the concentration after adsorption equilibrium, respectively. $\triangle C$ denotes the difference in

ion concentration after correction of the original solution; V_i indicates the solution volume; M shows the molar mass; m_0 represents the sample mineral mass.

When there are more cations adsorbed in coal, the electrical conductivity is obviously enhanced [57]. Generally speaking, the electric pulse breakdown of coal samples is mainly divided into surface fracturing and internal fracturing [58, 59]. The former is the failure of the performance of the insulating or weakly conducting regions of the coal under the action of a strong electric field, resulting in the rapid flow of current from the surface of coal sample; the latter is the electrical and thermal stresses generated by the passage of current from the conductive regions connected in the coal to destroy the plasma channels, leading to fractures in coal sample. These approaches cause new fractures or fragmentation in coal, which is favorable for the pore-fracture connectivity. The breakdown field E and the required energy W are calculated as follows:

$$E = \frac{U}{L} \tag{2}$$

$$W = \frac{1}{2} C U^2 \tag{3}$$

where U denotes the fracturing voltage of coal sample; L represents the length of the cylindrical coal sample; and C stands for the capacitance.

3.2. Characterization of pore-fracture

Considering the strong heterogeneity of coal, the pore-fracture after EPF was characterized by combining FS-SEM and AFM [14, 35]. Although all coal samples were polished, there were still a few scratches on their surfaces, so these areas should be avoided as much as possible during the scanning process. The surface of coal sample

was observed by the FS-SEM model Merlin manufactured by Carl Zeiss AG, Germany, to obtain the pore-fracture morphology and structure information through the detector (Fig. 3a). AFM, including an accurate data processing module, was adopted to quantify pore size distribution and porosity [45]. The AFM scanned images were processed by the first-order Flatten method in NanoScope Analysis software to reduce noise and thus facilitate the fine identification of pores in different ranges (Fig. 3b). To observe the spatial distribution characteristics of the coal surface, the three-dimensional coal samples were quantified by 3D Image in NanoScope Analysis (Fig. 3c), followed by line analysis by the Section module. Subsequently, the true pore size and depth distribution of the coal surface was marked by the Invert Height function in the Gwyddion software (Fig. 3d). Since the porosity obtained by the threshold method exists strong human interference factors, this paper adopts the watershed method to characterize the pore-fracture [20]. As a mathematical morphological segmentation method based on topological theory, the basic idea of the watershed theory is to consider the image as a topological morphology in the geological domain. In contrast, the boundary of catchment basin forms the watershed. Where the grayscale value of each point represents the height, the local minima and their influence area represent catchment basin. For tested coal samples, this can indicate the pore-fracture and matrix. The watershed theory can effectively evaluate coal samples with high anisotropy to obtain more comprehensive information on pore parameters.

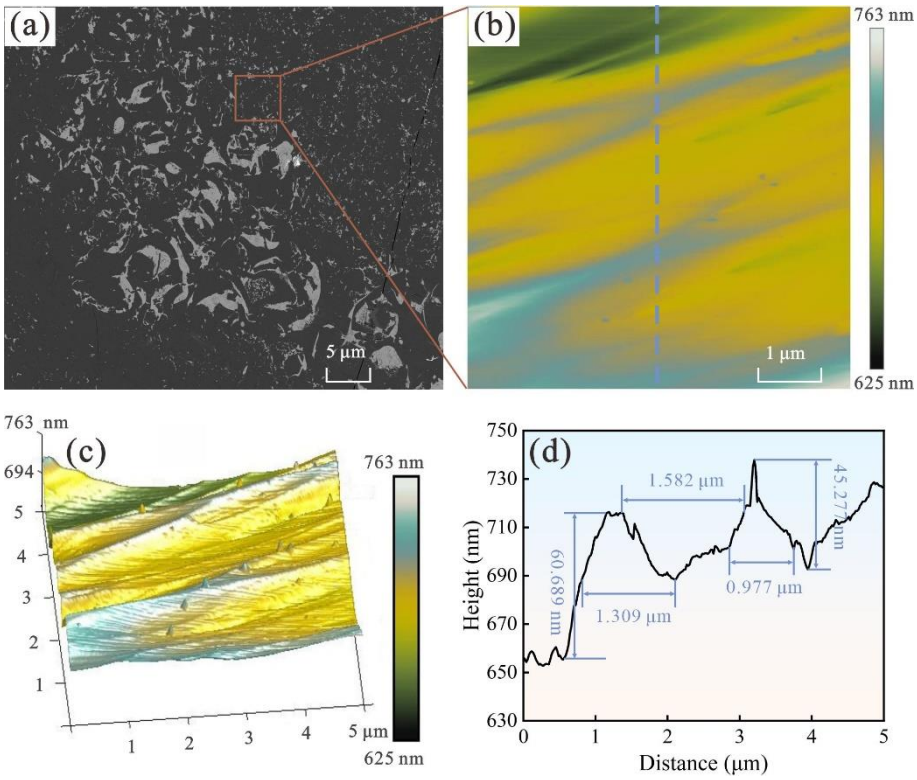

Fig. 3. Microscopic analysis of coal surface. (b) shows the AFM information of one slice of FS-SEM (a); (c) exhibits the 3D spatial distribution of (b); (d) indicates the slice analysis for (b).

3.3. Surface roughness calculation

AFM, with a noise level no greater than 0.3A, is a microscope that investigates surface structure and properties of coal samples by detecting the weak interatomic interaction forces between the surface and the probe [35, 60]. Amplitude is commonly used to study surface roughness because the amplitude parameters in the AFM scan images reflect the microscopic surface height distribution, statistical characteristics and extreme features of coal samples [14, 15]. The AFM images were smoothed using the Flatten function, followed by the analysis of coal sample roughness (including mean roughness R_a, root mean square roughness R_q, surface skewness R_{sk} and surface kurtosis

R_{ku}) by statistical functions. Among them, R_a can show the distance from the reference surface to the surface of coal sample, and its combination with R_q reflects the microscopic surface morphology changes. The symmetry of coal sample surface can be judged by R_{sk}, i.e., R_{sk}=0 indicates the symmetry of the surface distribution. R_{ku} is used to characterize the excess of the coal sample surface, which is generally related to the skewness. The calculation equations are as follows:

$$R_a = \frac{1}{N_x N_y} \sum_{i=1}^{N_x} \sum_{j=1}^{N_y} \left| z(i,j) - z_{mean} \right| \quad (4)$$

$$z_{mean} = \frac{1}{N_x N_y} \sum_{i=1}^{N_x} \sum_{j=1}^{N_y} z(i,j) \quad (5)$$

where N_x and N_y denote the number of scanned points in the x and y directions, respectively; Z and Z_{mean} represent the height of a single measurement point and the average height of all measurement points, respectively.

$$R_q = \sqrt{\frac{1}{N_x N_y} \sum_{i=1}^{N_x} \sum_{j=1}^{N_y} \left(z(i,j) - z_{mean} \right)^2} \quad (6)$$

$$R_{sk} = \frac{\frac{1}{N_x N_y} \sum_{i=1}^{N_x} \sum_{j=1}^{N_y} \left(z(i,j) - z_{mean} \right)^3}{R_q^3} \quad (7)$$

$$R_{ku} = \frac{\frac{1}{N_x N_y} \sum_{i=1}^{N_x} \sum_{j=1}^{N_y} \left(z(i,j) - z_{mean} \right)^4}{R_q^4} - 3 \quad (8)$$

3.4. Acquisition of mechanical parameters

In the PeakForce QNM™ mode, the cantilever oscillated Z piezoelectricity at a rate far below the resonant frequency of the probe to quantitatively characterize the mechanical properties [45]. To obtain a constant imaging force, the mechanical curve

of each pixel was obtained by measuring the sample surface through the deflection of the cantilever beam, and then the peak force of each tap was used as the control signal. Subsequently, the spring constant and deflection sensitivity of the probe were modified by standard methods to obtain the adhesion force for different coal samples [15, 20]. Since there were differences in the roughness of different measurement points resulting in an uneven baseline distribution, the baseline calibration in nanoscope analysis was used to obtain the correct adhesion force F_{adh}. The calculation equations are as follows:

$$F_{adh} = F_{tip} - \frac{4}{3} E^{*} \sqrt{Rd^{3}} \qquad (9)$$

where F_{tip} indicates the tip force; R shows the tip radius; and d represents the amount of sample deformation. The reduced modulus E^{*} is obtained as follows:

$$E^{*} = \left(\frac{1 - v_{s}^{2}}{E_{s}} + \frac{1 - v_{tip}^{2}}{E_{tip}} \right)^{-1} \qquad (10)$$

where v_s and v_{tip} denote the Poisson's ratio of coal sample and probe, respectively. E_s and E_{tip} indicate the Young's modulus of coal sample and probe, respectively.

4. Results and discussion

4.1. The adsorption of cations to coal

In the adsorption process, the closer the cation center is to the coal matrix, the stronger the adsorption capacity is in general [51]. As shown in Fig. 4, the medium- and high-rank coals exhibit similar adsorption trends for cations with different chemical valences, decreasing adsorption rates. The adsorption of CZ to cations reaches equilibrium at about 36 h (Fig. 4a), while QY reaches equilibrium 4 h earlier than CZ

(Fig. 4b), indicating that the adsorption of cations by medium-rank coal is stronger than that by high-rank coal. This is mainly due to the development of macropores and microfractures in QY than in CZ, resulting in relatively less resistance for cations to enter QY [61]. Moreover, the adsorption capacity of both coal samples for cations shows in the order of Fe^{3+} > Ca^{2+} > K^{+}. The amount of Fe^{3+} adsorbed at equilibrium is 2.6 times higher than that of K^{+} in CZ, which is mainly attributed to the fact that the higher the ionic valence, the smaller the radius of the hydrated ion, making the cation more easily adsorbed by the coal matrix.

As the reaction time increases, the adsorption of cations in medium- and high-rank coals reaches equilibrium. Due to the substantial increase in the number of conducting ions, the charge propagates more easily in the coal, similar to the research of Zhang et al. [55]. Additionally, coal contains inorganic minerals such as quartz, montmorillonite and kaolinite that possess a large lateral area and numerous free exchange ions [62], causing cations to be more easily adsorbed from solution into the coal.

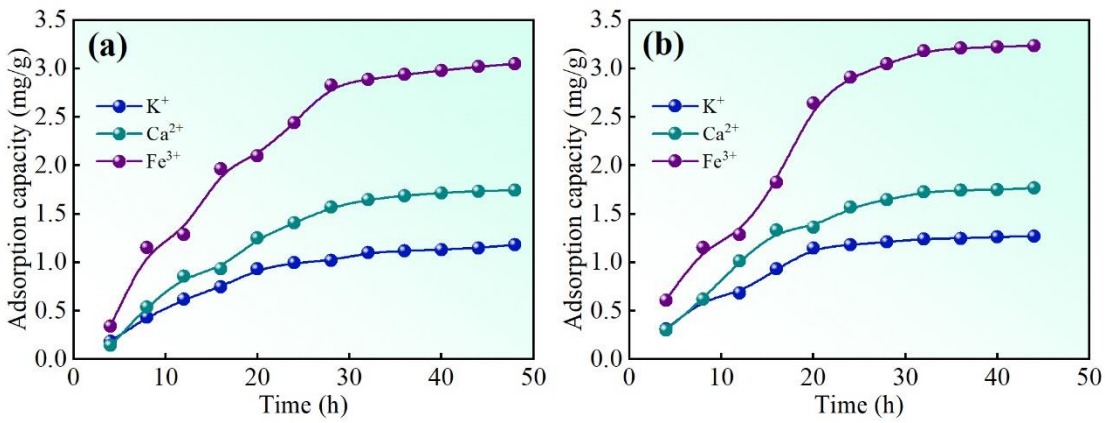

Fig. 4. The adsorption capacity of different cations at a concentration of 5 mol/L in coal with time. (a)-the coal sample CZ; (b)-the coal sample QY.

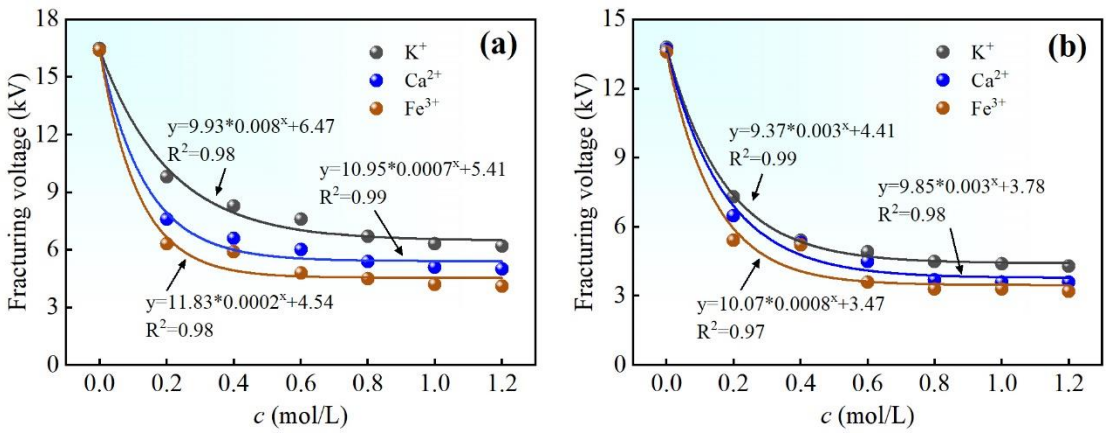

Fig. 5. Fracturing voltages after adsorption of different concentrations of cations in coal. The fracturing voltage of CZ (a) is generally higher than that of QY (b).

4.2. Breakdown field of EPF coal body

As a critical parameter of the EPF coal body, the voltage level controls the degree of coal fragmentation [57, 58]. As shown in Fig. 5, the fracturing voltage of CZ and QY decreases in a negative exponential pattern with the change of adsorption concentration of different cations. This is attributed to the fact that more ions go into pore-fracture as the solution concentration increases, leading to enhanced conductivity by connecting the insulating regions in coal [63]. CZ and QY show fracturing voltages of 16.5 kV and 13.8 kV, respectively, when no cations are adsorbed, indicating that medium-rank coal conducts electricity better than high-rank coal [64]. The fracturing voltage of CZ reaches equilibrium at the concentration of 1 mol/L for the three cations, lagging behind QY adsorbed cations by 0.2 mol/L. Additionally, CZ requires a fracturing voltage of 6.3 kV for adsorption of 1.2 mol/L K^+ (Fig. 5a), higher than that of 2.1 kV for adsorption of Fe^{3+}. While, A much lower voltage can be observed in the fracturing QY process (Fig. 5b), i.e., a fracturing voltage of only 3.2 kV is enough for QY with adsorbed 1.2

mol/L Fe^{3+}. The fracturing voltage variation trends of the two coal samples after adsorption of K^+ are greater than those of Ca^{2+} and Fe^{3+}, demonstrating that coal adsorption of cations with high valence is more likely to form plasma channels [59]. The higher the concentration of cation solution, the more plasma channels are easily generated in coal, which is very favored for EPF.

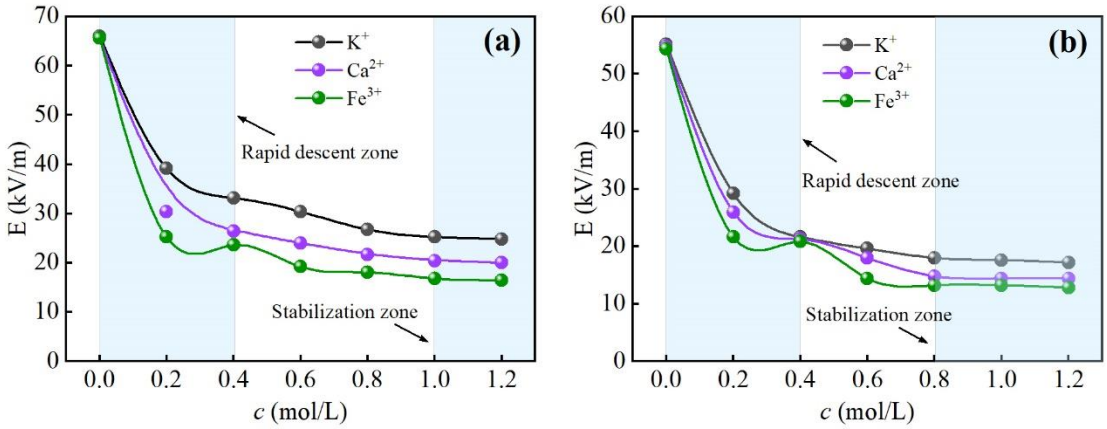

Fig. 6. Variation of electric pulse breakdown field with cation adsorption concentration in coal. With the increase of cation concentration, both the breakdown fields of CZ (a) and QY (b) experienced the trend of "rapid decrease-slow decrease-stabilization", and CZ lagged behind QY to reach the equilibrium state.

As illustrated in Fig. 6, the breakdown field in coal shows a trend of "rapid decrease-slow decrease-stabilization" with the cation adsorption concentration. In the original state, the breakdown field of QY is 0.8 times higher than that of CZ. The breakdown fields of 25.2 kV/m, 20.4 kV/m and 16.8 kV/m are exhibited when the breakdown voltages of CZ adsorbed 1mol/L K^+, Ca^{2+} and Fe^{3+} reach equilibrium (Fig. 5a and Fig. 6a), respectively. However, smaller breakdown fields are found in QY (Fig. 6b), that is, QY indicates breakdown fields of 17.6 kV/m, 14.4 kV/m and 132 kV/m at the same cation concentration conditions, respectively. This reveals that the diffusion of K^+, Ca^{2+}

and Fe^{3+} into the coal improves the electrical conductivity, causing the coal body to fracture more easily [51]. Moreover, with the increase of cation valence, the resistance to current flow in coal decreases, thus reducing the breakdown field [64]. During the whole fracturing process, the breakdown field of QY is always smaller than that of CZ, suggesting that the higher the metamorphism degree of coal, the greater the breakdown field variation.

For the energy change during EPF, the electric field energy required to break CZ is 1.4 times higher than QY (Fig. 7). When the breakdown field reaches the equilibrium state, the energy required for CZ with adsorbed K^+ is 2.3 times higher than that with adsorbed Fe^{3+} in the fracturing process (Fig. 6a and Fig. 7a). In contrast, less energies are required to fracture QY, with adsorption of K^+, Ca^{2+} and Fe^{3+} exhibiting electric field energies of 73.96 J, 51.84 J and 40.96 J (Fig. 7b), respectively. Notably, the electric field energy changes of QY adsorbed with different cations are smaller than those of CZ in the EPF process (Fig. 4 and Fig. 7), demonstrating that high-rank coal is more sensitive to adsorb different valence cations than medium-rank coal.

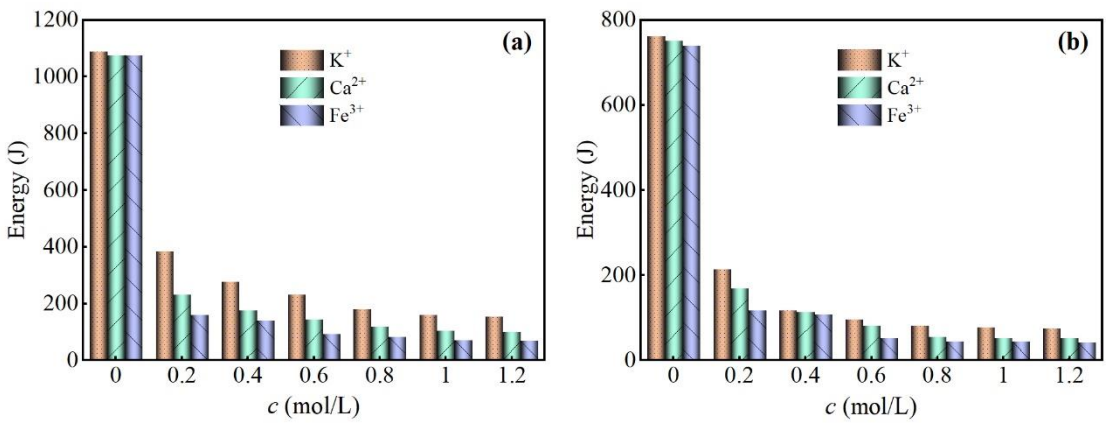

Fig. 7. Energy variations during EPF. The energy required for CZ (a) is greater than for QY (b) when different coals adsorbed cations reach the fracturing state.

When the electric field is applied to both ends of coal sample, the plasma channels in coal generate huge energy, resulting in the temperature rise of pore-fracture and throat [65, 66]. This not only affects the functional groups in coal but also generates large expansion stress, which makes the coal fracture under the action of the shock wave [61]. Since the degree of coal metamorphism can reflect the pore-fracture condition [4], the small pores in CZ are more developed than QY. However, cations are more likely to form plasma channels in the macropores and microfractures in coal, so the energy required to fracture QY is less than CZ.

4.3. Pore-fracture dynamic evolution induced by electrical pulses

4.3.1. Characteristics of macroscopic fractures

Due to the uneven development of cleats, exogenous fractures and inherited fractures in different coal seams [67, 68], the macroscopic damage characteristics of coal samples after EPF are obviously different. As illustrated in Fig. 8, the degree of EPF fragmentation of coal samples adsorbed with different valence cations is in the order of Fe^{3+} > Ca^{2+} > K^{+}, which is similar to the research results of Wang et al. [51]. In other words, the higher the cation valence, the easier the fragmentation of the EPF coal sample. Moreover, the degree of fragmentation of QY is greater than that of CZ regardless of which cation is adsorbed. Another interesting phenomenon is that the fracturing voltages of QY are all smaller than those of CZ, confirming that the cations are more likely to enter the pores and fractures of QY.

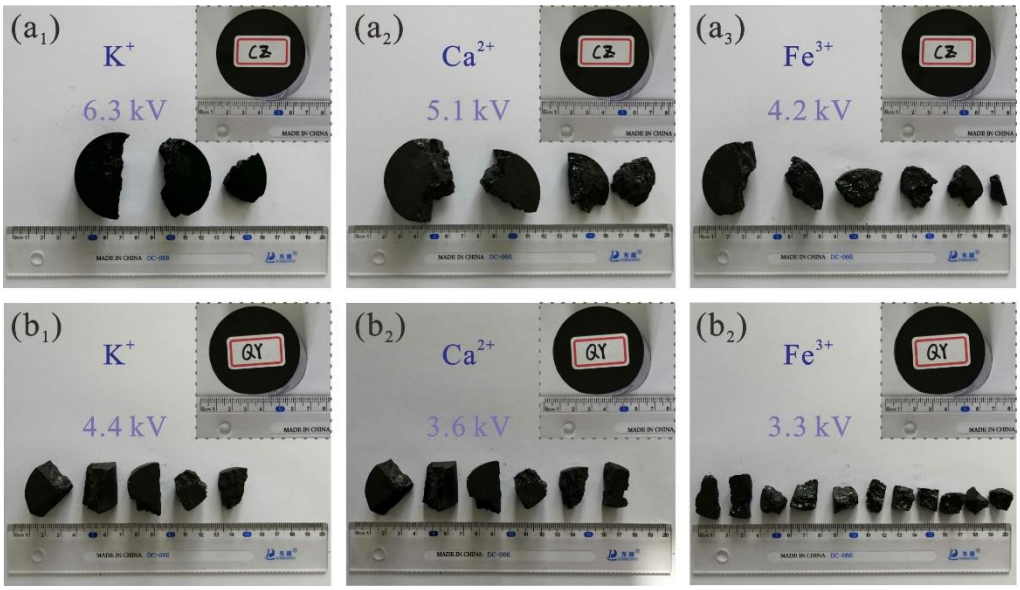

Fig. 8. Macroscopic damage characteristics of high-rank coal (a) and medium-rank coal (b) by EPF after adsorption of 1 mol/L different cations.

Coal, being a porous medium, exhibits different dielectric properties [64, 69]. Therefore, different forms of distortion occur under the action of electric fields [70]. Throughout the EPF process, the damage of coal is divided into three forms: (i) the strong stress wave generated by the current in the coal exceeds the shear strength leading to the penetration between the original fracture and the newly generated fracture; (ii) the accumulation of large amounts of energy in the plasma channel generates thermal expansion stress causing the coal to be burst; (iii) the collapse of the vacuoles formed by the cationic solution in the microfractures adds additional tensile stress. The overall surface area of the broken coal sample increases obviously, and some rock cuttings are formed. With the significant increase in the number of fractures, the pore-fracture connections at different scales become more diverse, which is very beneficial to methane desorption and fluid transport [34].

4.3.2. Surface morphological features observed by FS-SEM

FE-SEM, equipped with X-ray energy spectroscopy and high-performance cathodoluminescence, is often used to investigate the physical characteristics of coal because of the high-resolution secondary electron images that can be obtained for specific wavelength spectra [59, 71]. As depicted in Fig. 9, the surface morphology of coal sample can be clearly observed after the magnification of 20,000 times. The surface of the raw coal is relatively flat, and there are some minerals and nodules. Influenced by tectonic movement and magmatic thermal metamorphism, the surface structures of CZ and QY differ significantly (Fig. 9a and e). Clay minerals are clearly visible in CZ, mainly filled with kaolinite, with occasional pyrite particles. Some pores and microfractures can be observed in QY with regular fiber structure, which is related to coal seam being in the superposition zone of synclinal core and anticlinal wing [9].

After the action of electric pulse, the surfaces of coal samples adsorbed with different cations become uneven, and the pore-fractures of different shapes increase significantly. Many irregular pores can be observed in CZ of adsorbed K+ by the effect of EPF (Fig. 9b), while the slit-like pores are mainly in the adsorption of Ca^{2+} and Fe^{3+} (Fig. 9c and d). Additionally, QY adsorbed with K^{+} and Fe^{3+} forms many clustered pores (Fig. 9f and h), which is very beneficial to the connection between diffusion pores and seepage pores [58]. In particular, QY adsorbed with Fe^{3+} can also be clearly observed with many connected pores, enhancing the permeability of the coal [62]. Moreover, the pore-fractures of QY adsorbed with Ca^{2+} increase significantly (Fig. 9g), which provides a better condition for gas conversion from Knudsen diffusion to

Transition diffusion or Fick diffusion in coal. In conclusion, EPF action on the adsorbed cation coal samples significantly increases the pore-fracture network coverage, resulting in a significant improvement in connectivity.

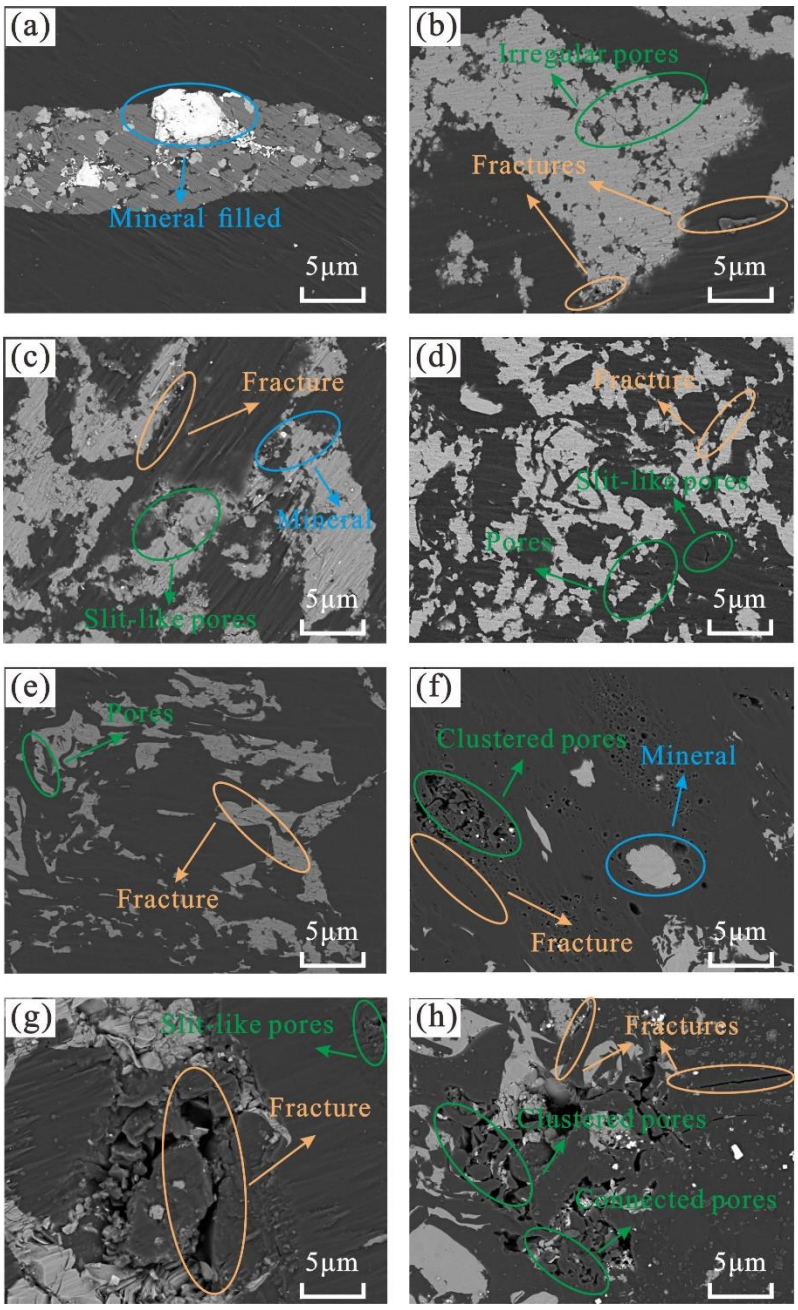

Fig. 9. Surface morphological characteristics of different coal samples after EPF observed by FE-SEM. For the high-rank coal CZ (a), the pore-fractures of adsorbed K^+ (b), Ca^{2+} (c) and Fe^{3+} (d) are obviously more than the original. The connectivity of the

original QY (e) is significantly lower than that of adsorbed K^+ (f), Ca^{2+} (g) and Fe^{3+} (h).

4.3.3. Quantification of pore changes after EPF by AFM

In order to accurately characterize the physical properties of coal, the watershed method was used to analyze the pore dynamics after EPF [20, 45]. According to the interaction effect of diffusion-seepage, the pore-fractures in coal were classified as super-micropores (< 2 nm), micropores (2–10 nm), mesopores (10–10^2 nm), macropores (10^2–10^3 nm), super-pores (10^3–10^4 nm) and microfractures (> 10^4 nm) [17]. Independent pores can be observed on the surface of the raw coal (Fig. 10a and e), mainly consisting of micropores, mesopores and macropores. It is obvious that pores of different scales are connected by EPF, leading to a significant increase in connectivity. As indicated in Fig. 10, the number of pores increases from 71 to 229 after the fracturing of CZ with adsorbed Fe^{3+} (Fig. 10a and d), especially increasing many cluster pores. Additionally, the pore number of QY with adsorbed cations varies from 65 to 185, with an average of 133 (Fig. 10e, f, g and h). The average pore size of CZ adsorbed cations increases with the increase of the valence, ranging from 72.36 to 112.9 nm. While, a larger range of average pore size variation can be observed in QY, with an increase of 61.77 nm. Moreover, the porosity of CZ increases from 4.1% to 27.4%, greater than that of QY from 6.7% to 14.5%, which is related to the different degree of coalification of the two coal samples [64]. The higher the degree of coalification, the greater the change in porosity after EPF.

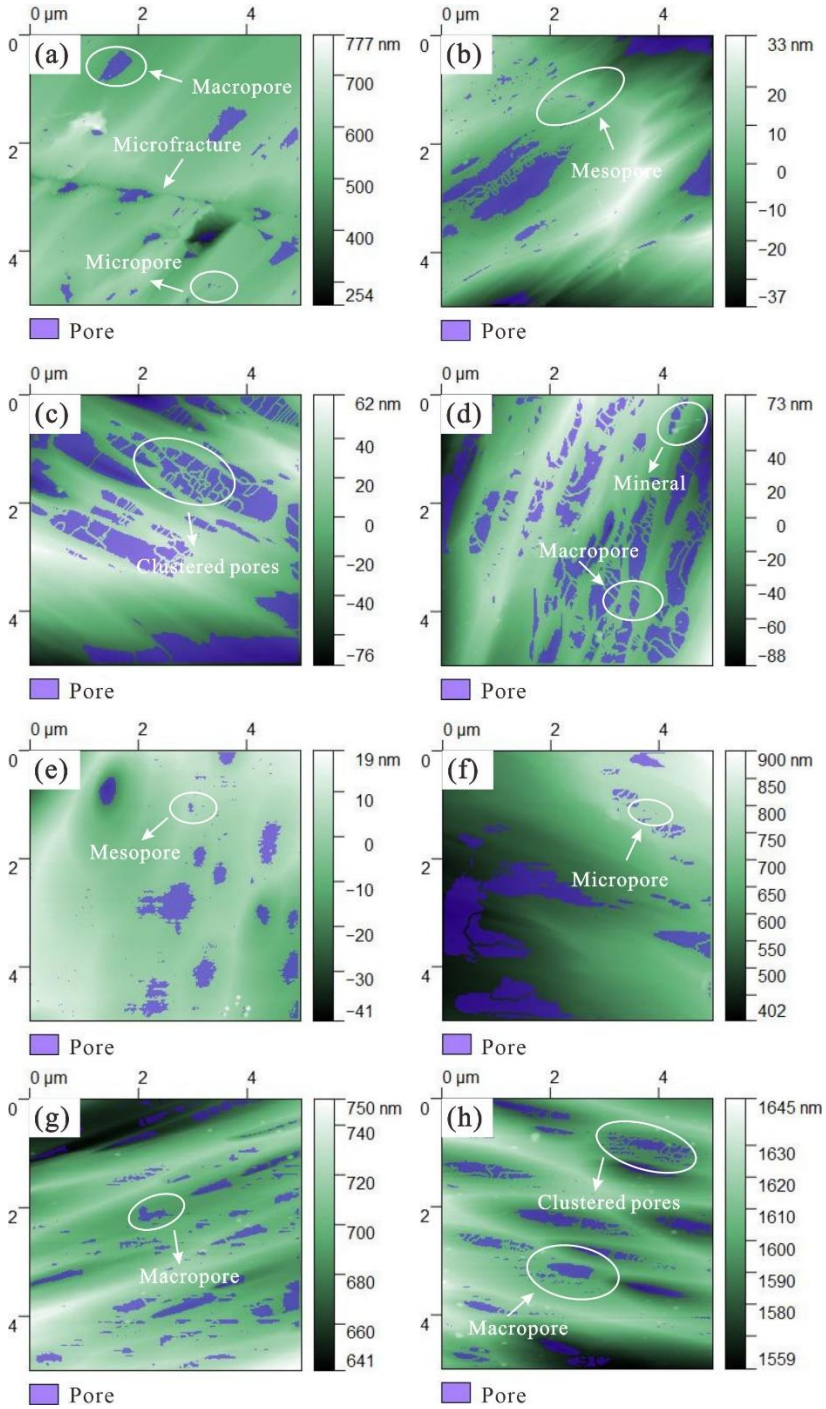

Fig. 10. Pore variations of coal adsorbed with different cations by EPF observed by AFM. (b), (c) and (d) denote CZ (a) with adsorbed K^+, Ca^{2+} and Fe^{3+}, respectively. (f), (g) and (h) represent QY (e) with adsorbed K^+, Ca^{2+} and Fe^{3+}, respectively.

During the whole process of EPF, the main contribution of macropores to the pore volume increases, resulting in a weaker resistance to gas transport in coal. Due to the

influence of heterogeneity and anisotropy, the pore variation in different areas of coal samples with adsorbed cations by EPF varies greatly. In general, EPF is more favorable to the production of CBM.

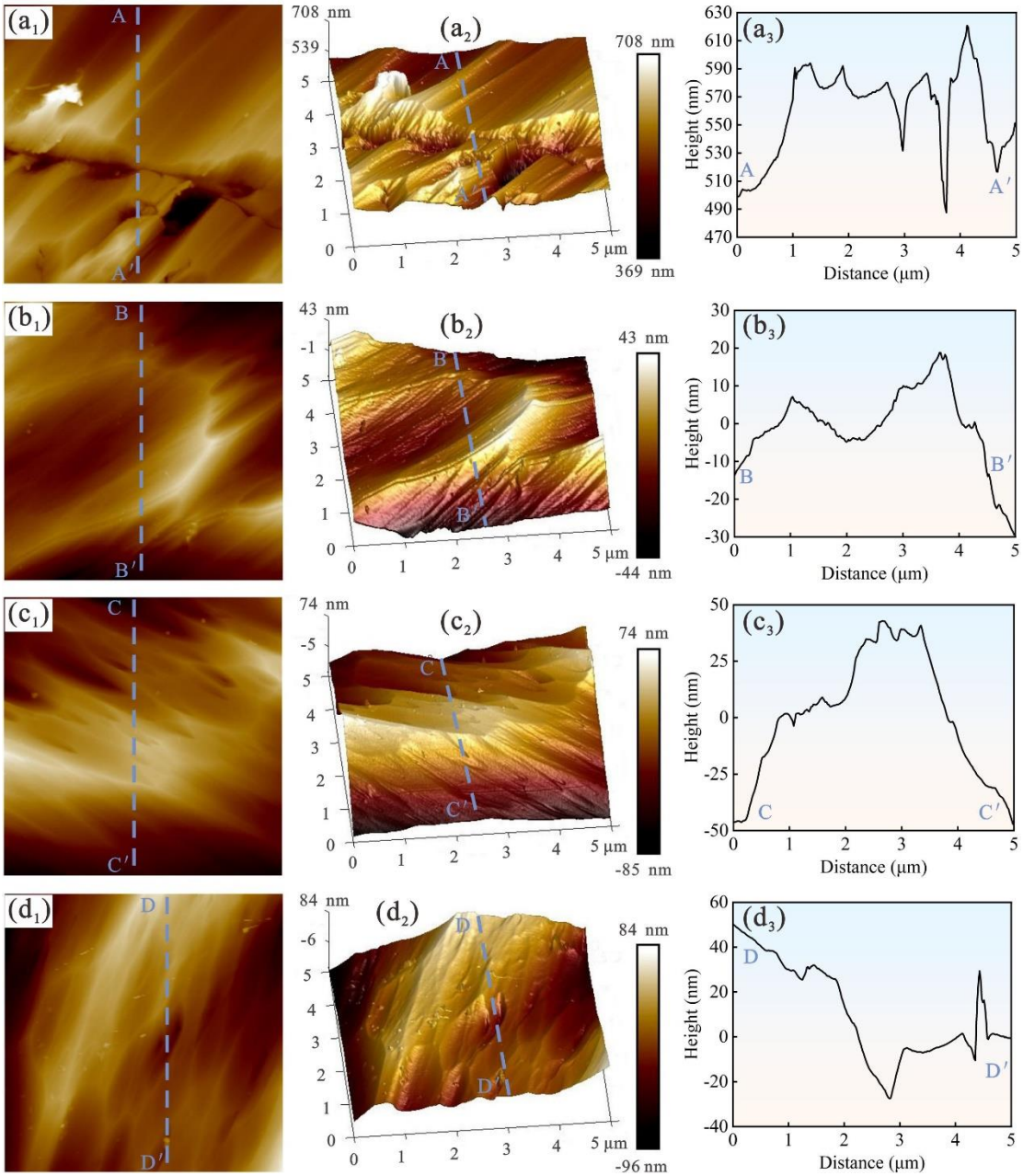

Fig. 11. Roughness variation of coal in two and three dimensions by AFM. (a), CZ; (b), CZ with adsorbed K^+; (c), CZ with adsorbed Ca^{2+}; (d), CZ with adsorbed Fe^{3+}.

4.4. Changes in surface roughness after EPF

As an essential index to characterize the microscopic morphology of objects [14], surface roughness plays a crucial role in reflecting contact angle, wettability and capillary resistance. Especially, 3D images can better visualize the spatial characteristics of coal. As depicted in Fig. 11, the roughness of coal changes significantly after the adsorption of different cations. The average of 256 points in a 5×5 μm area was extracted as the overall surface roughness to improve accuracy. The R_a of CZ with adsorbed K^+ decreases from 27 to 9.73 nm after EPF, with the R_q decreasing from 30.2 nm to 10.1 nm (Fig. 11a and b). This indicates that the surface fluctuations of coal are significantly less complex [20], i.e., there is a shift from rough to smooth, leading to significantly lower resistance to methane transport. Using the same characterization method, the R_a of QY adsorbed with different cations ranges from 4.94 to 28.8 nm, demonstrating a greater average roughness variation. Since a small surface roughness undulation leads to a large R_q change, the root mean square roughness is more sensitive to pore-fracture changes [45]. The variation of R_q of QY varies from 2.59 to 37.4 nm, illustrating that the roughness change of QY with adsorbed cations after EPF is greater than that of CZ.

For the surface skewness, the R_{sk} of CZ adsorbed with different cations by EPF ranges from -0.82 to -0.17 (Fig. 11), implying that there are more regions in CZ with surface undulations above the average roughness. Since R_{sk} is negative throughout the EPF process, the surface height of CZ exhibits a normal distribution skewed to the left of the y-axis [20]. Additionally, the R_{ku} of CZ adsorbed with different cations ranges

from 1.92 to 3.6, indicating that the surface height is concentrated around the mean value [15]. Another more interesting phenomenon is the shift from positive to negative values of R_{sk} for QY adsorbed with different valence cations (i.e., from 1.1 to -0.32 gradually), which indicates the change of coal surface height from the right-skewed normal distribution to the left-skewed one [35]. Moreover, the area where the surface height of QY adsorbed cation is below the average value gradually increases with the increase of the chemical valence.

4.5. Micromechanical property

The adhesion force, reflecting the surface energy of the coal sample, is essential for evaluating the adsorption properties of coal [14, 20]. Due to the presence of van der Waals force, electrostatic force and strong interaction force, the adhesion forces on the coal surface vary in various ways [45]. Fig. 12 shows the three-dimensional distribution of the adhesion force of QY adsorbed with different cations after EPF. the adhesion force of QY ranges from -2.4 to 21.8 nN (Fig. 12a), which is strong for the adsorption of methane on the matrix surface [72, 73]. The adhesion force of QY with adsorbed cations shows an overall decreasing trend, ranging from -0.9 to 9.1 nN (Fig. 12b, c and d). It is noteworthy that the adhesion force of QY for adsorbed Fe^{3+} is 3-6 times higher than that for adsorbed K^{+} and Ca^{2+}, mainly due to the pore-fracture in the sample being filled with minerals. Using similar characterization methods, the adhesion force of CZ varies between 0.9 and 20.7 nN. Overall, the adhesion force of CZ is smaller than that of QY. This is mainly due to the weakening of intermolecular forces on the coal surface with the deepening of coalification, resulting in a decrease in adhesion force [7].

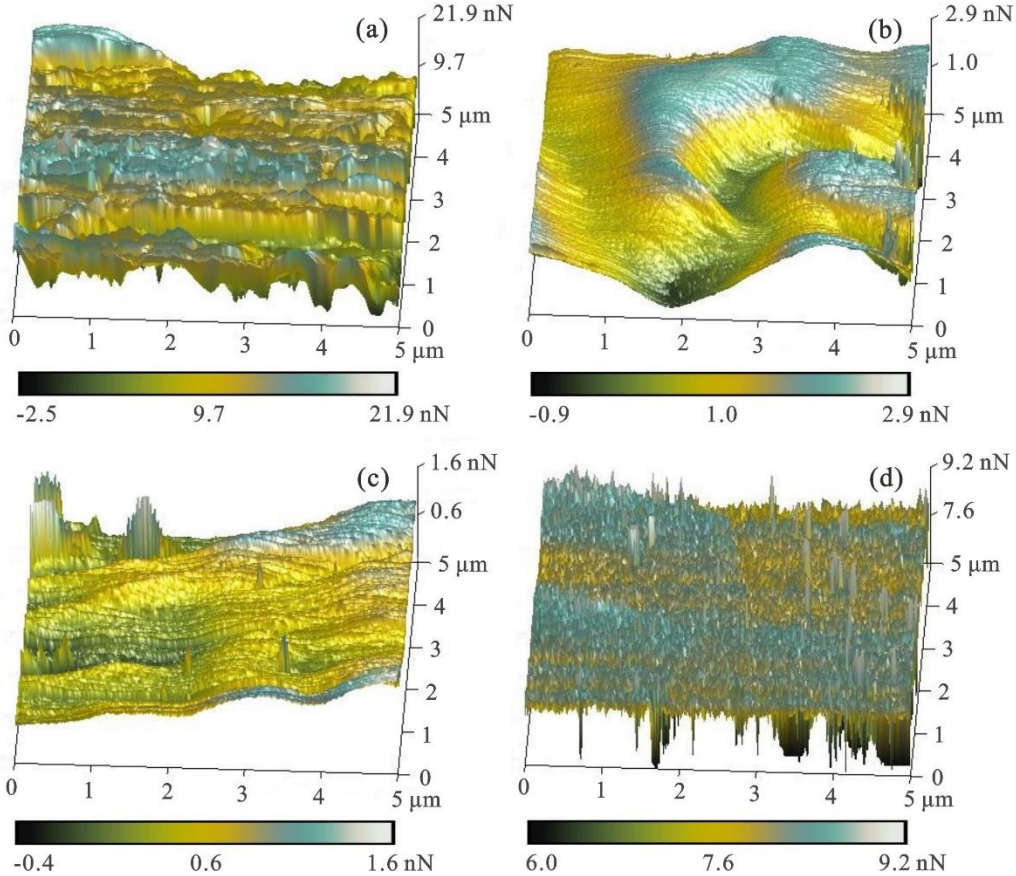

Fig. 12. Three-dimensional distribution of adhesion force. (a), QY; (b), QY with adsorbed K^+; (c), QY with adsorbed Ca^{2+}; (d), QY with adsorbed Fe^{3+}.

To investigate the distribution pattern of the micromechanics, Fig. 13 shows the frequency distribution of the adhesion force in Fig. 12. The adhesion force of QY is relatively dispersed, with the most frequency distribution of 13.1nN (Fig. 13a). After the adsorption of cations, the adhesion force distribution of QY becomes relatively concentrated. With the increase of the cation valence, the concentration of the adhesion force distribution increases (Fig. 13b, c and d). Particularly, the adhesion force of QY with adsorbed Fe^{3+} is mainly distributed at 8.1 nN, accounting for nearly 1% (Fig. 13d). This indicates that the heterogeneity of the adhesion force of coal adsorbed with different cations after EPF is diminished, which is favorable for better fluid transport

in the fracture channels [14]. For coal seams containing abundant groundwater, different cations in solution can lead to differences in the adhesion of coal [45], which provides new insights into the differences in gas production mechanisms of CBM wells in the same coal seam from different regions. Furthermore, different concentrations of cations also cause changes in adhesion, which gives good indications for the fluid geology of CBM production in different sedimentary environments.

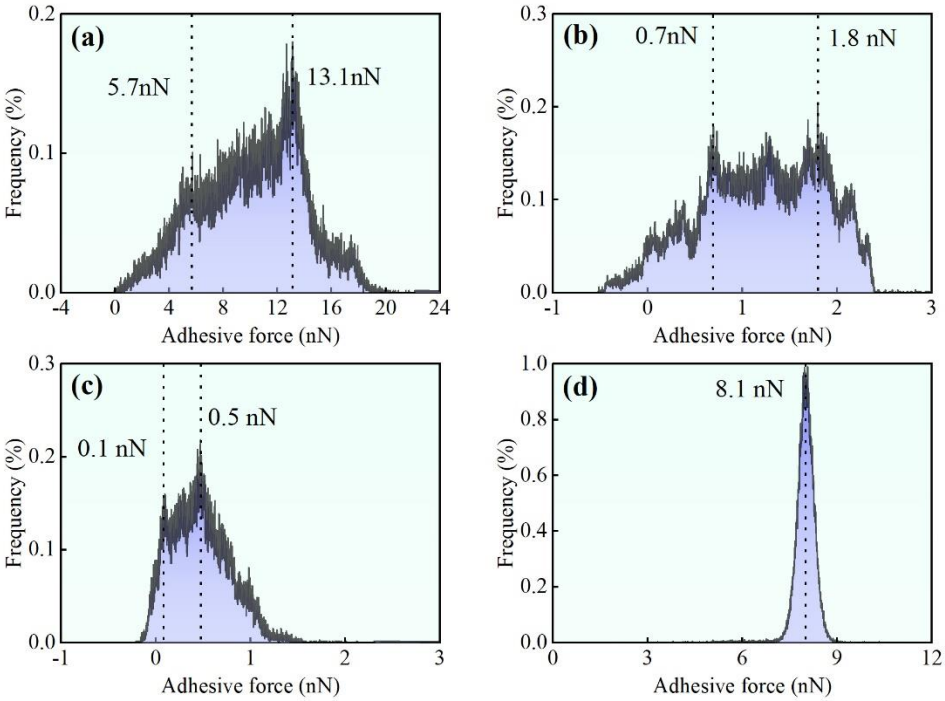

Fig. 13. Frequency distribution of adhesive forces in different ranges.

5. Conclusions

In this work, the breakdown field response processes of medium- and high-rank coals adsorbed with different cations after EPF were investigated, followed by the analysis of microscopic pore-fracture evolution and surface roughness changes. To evaluate the micromechanical properties of coal, the distribution characteristics of the adhesion with increasing cation valence were characterized. The following conclusions

are drawn:

(1) With the increase of cation concentration, the breakdown field in coal shows a trend of "rapid decrease-slow decrease-stabilization". During the whole EPF period, the electric field energy change of QY adsorbed with different cations is smaller than that of CZ, demonstrating that high-rank coal is more sensitive to adsorb different valence cations than medium-rank coal.

(2) Affected by EPF, the average pore size of CZ adsorbed cations increases with the increase of the valence, ranging from 72.36 to 112.9 nm. While, a larger range of average pore size variation can be observed in QY, with an increase of 61.77 nm. Moreover, the porosity of CZ increases from 4.1% to 27.4%, greater than that of QY from 6.7% to 14.5%.

(3) The R_a of CZ with adsorbed K^+ decreases from 27 to 9.73 nm after EPF, with the R_q decreasing from 30.2 nm to 10.1 nm. For the surface skewness, the R_{sk} of QY adsorbed with different valence cations shifts from positive to negative values, which reflects the change of coal surface height from the right-skewed normal distribution to the left-skewed one.

(4) The adhesion force of QY for adsorbed Fe^{3+} is 3-6 times higher than that for adsorbed K^+ and Ca^{2+}, mainly due to the pore-fracture in the sample being filled with minerals. With the increase of the cation valence, the concentration of the adhesion force distribution increases, which is favorable for better fluid transport in the fracture channels.

CRediT authorship contribution statement

Qifeng Jia: Investigation, Writing - original draft, Methodology, Data curation. **Dameng Liu**: Supervision, Conceptualization, Visualization, Funding acquisition. **Yidong Cai**: Formal analysis, Supervision, Funding acquisition. **Yingfang Zhou**: Supervision, Validation, Writing - review & editing. **Zheng Zhao**: Data curation, Image Processing. **Yanqing Yang**: Resources, Investigation.

Declaration of Competing interests

The authors declare that they have no known competing financial interests or personal relationships that could have appeared to influence the work reported in this paper.

Acknowledgements

This research was funded by the National Natural Science Foundation of China (grant nos. 41830427, 42130806 and 41922016), 2021 Graduate Innovation Fund Project of China University of Geosciences, Beijing (grant no. ZD2021YC035) and the Fundamental Research Funds for Central Universities (grant no. 2-9-2021-067). We are very grateful to the reviewers and editors for their valuable comments and suggestions.

Nomenclature

Γ Adsorption capacity [mg/g]

C_i Initial concentration of the cation solution [mol/L]

C_e Concentration after adsorption equilibrium [mol/L]

$\triangle C$ Difference in ion concentration after correction of the original solution [mol/L]

V_i	Solution volume [L]
M	Molar mass [g/mol]
m_0	Sample mineral mass [g]
E	Breakdown field [kV/m]
W	Electric field energy [J]
U	Fracturing voltage [kV]
L	Length of coal sample [kV]
C	Capacitance [F]
R_a	Mean roughness [nm]
R_q	Root mean square roughness [nm]
R_{sk}	Surface skewness
R_{ku}	Surface kurtosis
N_x	The number of scanned points in the *x* direction
N_y	The number of scanned points in the *y* direction
Z	The height of a single measurement point [nm]
Z_{mean}	The average height of all measurement points [nm]
F_{adh}	Adhesion force [nN]
F_{tip}	Tip force [nN]
R	Tip radius [nm]
d	Amount of sample deformation [nm]
E^*	Reduced modulus [nm]
v_s	The Poisson's ratio of coal sample

ν_{tip} The Poisson's ratio of probe

E_s The Young's modulus of coal sample [GPa]

E_{tip} The Young's modulus of probe [GPa]

References

[1] Li Y, Pan S, Ning S, Shao L, Jing Z, Wang Z. Coal measure metallogeny: Metallogenic system and implication for resource and environment. Sci China Earth Sci 2022; 65.

[2] Li Y, Wang Z, Tang S, Elsworth D. Re-evaluating adsorbed and free methane content in coal and its ad- and desorption processes analysis. Chem Eng J 2022;428:131946

[3] Zheng S, Yao Y, Liu D, Cai Y, Liu Y. Characterizations of full-scale pore size distribution, porosity and permeability of coals: A novel methodology by nuclear magnetic resonance and fractal analysis theory. Int J Coal Geol 2018;196:148-158.

[4] Liu D, Zou Z, Cai Y, Qiu Y, Zhou Y, He S. An updated study on CH4 isothermal adsorption and isosteric adsorption heat behaviors of variable rank coals. J Nat Gas Sci Eng 2021;89:103899.

[5] Xu Y, Lun Z, Pan Z, Wang H, Zhou X, Zhao C, et al. Occurrence space and state of shale oil: A review. J Petrol Sci Eng 2022;211:110183.

[6] Zheng S, Yao Y, Liu D, Cai Y, Liu Y, Li X. Nuclear magnetic resonance T2 cutoffs of coals: A novel method by multifractal analysis theory. Fuel 2019;241:715-724.

[7] Pan J, Zhu H, Hou Q, Wang H, Wang S. Macromolecular and pore structures of Chinese tectonically deformed coal studied by atomic force microscopy. Fuel 2015;139:94-101.

[8] Kang J, Wan R, Zhou F, Liu Y, Li Z, Yin Y. Effects of supercritical CO2 extraction on adsorption characteristics of methane on different types of coals. Chem Eng J 2020;388:123449.

[9] Li Z, Liu D, Ranjith PG, Cai Y, Wang Y. Geological controls on variable gas concentrations: A

case study of the northern Gujiao Block, northwestern Qinshui Basin, China. Mar Petrol Geol 2018;92:582-596.

[10] Wang Y, Liu D, Cai Y, Yao Y, Zhou Y. Evaluation of structured coal evolution and distribution by geophysical logging methods in the Gujiao Block, northwest Qinshui basin, China. J Nat Gas Sci Eng 2018;51:210-222.

[11] Yu S, Bo J, Ming L, Chenliang H, Shaochun X. A review on pore-fractures in tectonically deformed coals. Fuel 2020;278:118248.

[12] Li Y, Zhang C, Tang D, Gan Q, Niu X, Wang K, et al. Coal pore size distributions controlled by the coalification process: An experimental study of coals from the Junggar, Ordos and Qinshui basins in China. Fuel 2017;206:352-363.

[13] Li Y, Yang J, Pan Z, Meng S, Wang K, Niu X. Unconventional Natural Gas Accumulations in Stacked Deposits: A Discussion of Upper Paleozoic Coal- Bearing Strata in the East Margin of the Ordos Basin, China. Acta Geol Sin - Engl 2019;93(1):111-129.

[14] Li Y, Yang J, Pan Z, Tong W. Nanoscale pore structure and mechanical property analysis of coal: An insight combining AFM and SEM images. Fuel 2020;260:116352.

[15] Eliyahu M, Emmanuel S, Day-Stirrat RJ, Macaulay CI. Mechanical properties of organic matter in shales mapped at the nanometer scale. Mar Petrol Geol 2015;59:294-304.

[16] Li Q, Liu D, Cai Y, Zhao B, Lu Y, Zhou Y. Effects of natural micro-fracture morphology, temperature and pressure on fluid flow in coals through fractal theory combined with lattice Boltzmann method. Fuel 2021;286:119468.

[17] Cai Y, Li Q, Liu D, Zhou Y, Lv D. Insights into matrix compressibility of coals by mercury intrusion porosimetry and N2 adsorption. Int J Coal Geol 2018;200:199-212.

[18] Xie J, Gao M, Zhang R, Liu J, Lu T, Wang M. Gas flow characteristics of coal samples with different levels of fracture network complexity under triaxial loading and unloading conditions. J Petrol Sci Eng 2020;195:107606.

[19] Lu J, Yin G, Zhang D, Gao H, Li C, Li M. True triaxial strength and failure characteristics of cubic coal and sandstone under different loading paths. Int J Rock Mech Min 2020;135:104439.

[20] Zhao S, Li Y, Wang Y, Ma Z, Huang X. Quantitative study on coal and shale pore structure and surface roughness based on atomic force microscopy and image processing. Fuel 2019;244:78-90.

[21] Kang J, Elsworth D, Fu X, Liang S, Chen H. Contribution of thermal expansion on gas adsorption to coal sorption-induced swelling. Chem Eng J 2022;432:134427.

[22] Chen Y, Ma D, Xia Y, Guo C, Yang F, Shao K. Characteristics of the mud shale reservoirs in coal-bearing strata and resources evaluation in the eastern margin of the Ordos Basin, China. Energ Explor Exploit 2019;38(2):372-405.

[23] Chen Y, Tang D, Xu H, Tao S, Li S, Yang G, et al. Pore and fracture characteristics of different rank coals in the eastern margin of the Ordos Basin, China. J Nat Gas Sci Eng 2015;26:1264-1277.

[24] Song D, Liu X, He X, Nie B, Wang W. Investigation on the surface electrical characteristics of coal and influencing factors. Fuel 2021;287:119551.

[25] Xie L, You Q, Wang E, Li T, Song Y. Quantitative characterization of pore size and structural features in ultra-low permeability reservoirs based on X-ray computed tomography. J Petrol Sci Eng 2022;208:107606.

[26] Wang C, Wu K, Scott GG, Akisanya AR, Gan Q, Zhou Y. A New Method for Pore Structure

Quantification and Pore Network Extraction from SEM Images. Energ Fuel 2019;34(1):82-94.

[27] Li W, Nan Y, You Q, Jin Z. CO2 solubility in brine in silica nanopores in relation to geological CO2 sequestration in tight formations: Effect of salinity and pH. Chem Eng J 2021;411:127626.

[28] Kang J, Fu X, Li X, Liang S. Nitrogen injection to enhance methane and water production: An experimental study using the LF-NMR relaxation method. Int J Coal Geol 2019;211:103228.

[29] Tian X, Song D, He X, Liu H, Wang W, Li Z. Investigation of micro-surface potential of coals with different metamorphism by AFM. Measurement 2021;172:108915.

[30] Zhou Y, Hatzignatiou DG, Helland JO. On the estimation of CO_2 capillary entry pressure: Implications on geological CO_2 storage. Int J Greenh Gas Con 2017;63:26-36.

[31] Zhu L, Ma Y, Cai J, Zhang C, Wu S, Zhou X. Key factors of marine shale conductivity in southern China—Part II: The influence of pore system and the development direction of shale gas saturation models. J Petrol Sci Eng 2022;209:109516.

[32] Liu Z, Liu D, Cai Y, Qiu Y. Permeability, mineral and pore characteristics of coals response to acid treatment by NMR and QEMSCAN: Insights into acid sensitivity mechanism. J Petrol Sci Eng 2021;198:108205.

[33] Takise K, Manabe S, Muraguchi K, Higo T, Ogo S, Sekine Y. Anchoring effect and oxygen redox property of Co/La 0.7 Sr 0.3 AlO 3-δ perovskite catalyst on toluene steam reforming reaction. Appl Catal A-gen 2017;538:181-189.

[34] Lu Y, Liu D, Cai Y, Li Q, Zhou Y. Spontaneous imbibition in coal with in-situ dynamic micro-CT imaging. J Petrol Sci Eng 2022;208:109296.

[35] Chen S, Li X, Chen S, Wang Y, Gong Z, Zhang Y. A new application of atomic force microscopy in the characterization of pore structure and pore contribution in shale gas reservoirs. J Nat Gas

Sci Eng 2021;88:103802.

[36] Zhao Y, Wang C, Ning L, Zhao H, Bi J. Pore and fracture development in coal under stress conditions based on nuclear magnetic resonance and fractal theory. Fuel 2022;309:122112.

[37] Yang Q, Xue J, Li W, Hu B, Ma Q, Zhan K, et al. Reconstructions of supercritical CO2 adsorption isotherms and absolute adsorption estimation in nanoporous coals considering volumetric effects and varying adsorbed phase densities. Chem Eng J 2022;433:133492.

[38] Zeng K, Lu T, Jiang P, Zhou B, Xu R. Methane adsorption capacity measurement in shale matrix nanopores at high pressure by low-field NMR and molecular simulation. Chem Eng J 2022;430:133151.

[39] Takise K, Sato A, Muraguchi K, Ogo S, Sekine Y. Steam reforming of aromatic hydrocarbon at low temperature in electric field. Appl Catal A-gen 2019;573:56-63.

[40] Kutchko BG, Goodman AL, Rosenbaum E, Natesakhawat S, Wagner K. Characterization of coal before and after supercritical CO 2 exposure via feature relocation using field-emission scanning electron microscopy. Fuel 2013;107:777-786.

[41] Zhang M, Duan C, Li G, Fu X, Zhong Q, Liu H, et al. Determinations of the multifractal characteristics of the pore structures of low-, middle-, and high-rank coal using high-pressure mercury injection. J Petrol Sci Eng 2021;203:108656.

[42] O'Neill KT, Birt B, Hopper T. Borehole measurements of adsorbed gas content in coals using stimulated diffusion nuclear magnetic resonance. Int J Coal Geol 2021;247:103845.

[43] Zhang X, Lin B, Shen J. Experimental research on the effect of plasma on the pore-fracture structures and adsorption-desorption of coal body. Fuel 2022;307:121809.

[44] Zhao Y, Sun Y, Yuan L, Xu Q. Impact of nanopore structure on coal strength: A study based on

synchrotron radiation nano-CT. Results Phys 2020;17:103029.

[45] Lu Y, Liu D, Cai Y, Gao C, Jia Q, Zhou Y. AFM measurement of roughness, adhesive force and wettability in various rank coal samples from Qinshui and Junggar basin, China. Fuel 2022;317:123556.

[46] Tian X, Song D, He X, Khan M, Li Z, Liu H, et al. Presenting in-situ AFM investigations for the evolution of micro-surface topography and elastic modulus of rock under variable loads. Eng Fract Mech 2021;258:108107.

[47] Liu D, Yao Y, Chang Y. Measurement of adsorption phase densities with respect to different pressure: Potential application for determination of free and adsorbed methane in coalbed methane reservoir. Chem Eng J 2022;446:137103.

[48] Tian X, Song D, He X, Li Z, Liu H, Wang W. Investigation on micro-surface adhesion of coals and implications for gas occurrence and coal and gas outburst mechanism. J Nat Gas Sci Eng 2021;94:104115.

[49] Liu D, Yao Y, Wang H. Structural compartmentalization and its relationships with gas accumulation and gas production in the Zhengzhuang Field, southern Qinshui Basin. Int J Coal Geol 2022;259:104055.

[50] Zhou S, Yan D, Tang J, Pan Z. Abrupt change of pore system in lacustrine shales at oil- and gas-maturity during catagenesis. Int J Coal Geol 2020;228:103557.

[51] Wang Y, Yang W, Lin B, Yan F. Effects of different conductive ions on pore-structure evolution of medium- and high-rank coal bodies induced by electric pulses. Fuel 2021;293:120437.

[52] Moura H, Suárez-Ruiz I, Marques MM, Ribeiro J, Cunha PP, Flores D. Influence of magmatic fluids on the organic and inorganic fractions of coals from the Peñarroya-Belmez-Espiel Basin

(Spain). Int J Coal Geol 2021;235:103679.

[53] Sekine Y, Sakajiri K, Kikuchi E, Matsukata M. Release behavior of trace elements from coal during high-temperature processing. Powder Technol 2008;180(1-2):210-215.

[54] Zhao W, Su X, Zhang Y, Xia D, Hou S, Zhou Y, et al. Microbial electrolysis enhanced bioconversion of coal to methane compared with anaerobic digestion: Insights into differences in metabolic pathways. Energ Convers Manage 2022;259:115553.

[55] Zhang X, Lin B, Zhu C, Yan F, Liu T, Liu T, et al. Petrophysical variation of coal treated by cyclic high-voltage electrical pulse for coalbed methane recovery. J Petrol Sci Eng 2019;178:795-804.

[56] Zhu C, Lu X, Gao Z, Yan F, Guo C, Zhang X. Effect of high-voltage thermal breakdown on pore characteristics of coal. Int J Min Sci Techno 2017;27(6):1051-1055.

[57] Yan F, Lin B, Zhu C, Zhou Y, Liu X, Guo C, et al. Experimental investigation on anthracite coal fragmentation by high-voltage electrical pulses in the air condition: Effect of breakdown voltage. Fuel 2016;183:583-592.

[58] Zhang X, Lin B, Yang W, Shen C. Experimental study on the influence of energy conversion in the process of load coal plasma breakdown. Energy 2021;218:119469.

[59] Ni Z, Lin B, Zhang X, Cao X, Zhong L, Gao Y. Experimental study on the effect of high-voltage electrical pulses on the nanoscale pore structure of coal. Fuel 2021;306:121621.

[60] Liu X, Nie B, Wang W, Wang Z, Zhang L. The use of AFM in quantitative analysis of pore characteristics in coal and coal-bearing shale. Mar Petrol Geol 2019;105:331-337.

[61] Zhang X, Lin B, Zhu C, Wang Y, Guo C, Kong J. Improvement of the electrical disintegration of coal sample with different concentrations of NaCl solution. Fuel 2018;222:695-704.

[62] Wang Y, Yang W, Yan F, Lin B, Liu T, Zhou Q. Evolution of the Pore and Fracture Microstructure Inside Coal Impacted by a High-Voltage Electric Pulse after AlCl3 Solution Treatment. Energ Fuel 2021;35(22):18484-18494.

[63] Huo X, Zuo W, Shi F, Huang W. Coal middling retreatment using high voltage pulse technique. Part 1: Experimental findings. Fuel 2022;314:123066.

[64] Zhang X, Lin B, Li Y, Zhu C, Kong J, Li Y. Enhancement effect of NaCl solution on pore structure of coal with high-voltage electrical pulse treatment. Fuel 2019;235:744-752.

[65] Zhang X, Lin B, Li Y. Experimental study on the effects of electrode materials on coal breaking by plasma. Fuel 2020;270:117085.

[66] Yan F, Xu J, Lin B, Peng S, Zou Q, Zhang X. Changes in pore structure and permeability of anthracite coal before and after high-voltage electrical pulses treatment. Powder Technol 2019;343:560-567.

[67] Li Z, Liu D, Cai Y, Wang Y, Teng J. Adsorption pore structure and its fractal characteristics of coals by N2 adsorption/desorption and FESEM image analyses. Fuel 2019;257:116031.

[68] Liu P, Liu A, Zhong F, Jiang Y, Li J. Pore/fracture structure and gas permeability alterations induced by ultrasound treatment in coal and its application to enhanced coalbed methane recovery. J Petrol Sci Eng 2021;205:108862.

[69] Liu Z, Liu D, Cai Y, Yao Y, Pan Z, Zhou Y. Application of nuclear magnetic resonance (NMR) in coalbed methane and shale reservoirs: A review. Int J Coal Geol 2020;218:103261.

[70] Zhang X, Lin B, Li Y, Zhu C. Experimental study on the effect of coal thickness and breakdown voltage on energy conversion during electrical disintegration. Fuel 2020;259:116135.

[71] Yan F, Xu J, Lin B, Peng S, Zou Q, Zhang X. Effect of moisture content on structural evolution

characteristics of bituminous coal subjected to high-voltage electrical pulses. Fuel 2019;241:571-578.

[72] Gui X, Xing Y, Rong G, Cao Y, Liu J. Interaction forces between coal and kaolinite particles measured by atomic force microscopy. Powder Technol 2016;301:349-355.

[73] Li Y, Chen J, Elsworth D, Pan Z, Ma X. Nanoscale mechanical property variations concerning mineral composition and contact of marine shale. Geosci Front 2022;13:101405.

AFM characterization of physical properties in coal adsorbed with different cations induced by electric pulse fracturing

Qifeng Jia [a,b,c], Dameng Liu [a,b,*], Yidong Cai [a,b], Yingfang Zhou [c,d], Zheng Zhao [a,b], Yanqing Yang [e]

[a] *School of Energy Resources, China University of Geosciences, Beijing 100083, China*

[b] *Coal Reservoir Laboratory of National Engineering Research Center of CBM Development & Utilization, China University of Geosciences, Beijing 100083, China*

[c] *School of Engineering, Fraser Noble Building, King's College, University of Aberdeen, AB24 3UE Aberdeen, UK*

[d] *Department of Energy Resources, University of Stavanger, Stavanger, 4021, Norway*

[e] *Shanxi Lanyan Coalbed Methane Engineering Research Co., Ltd., Jincheng 048000, China*

* Corresponding author at: School of Energy Resources, China University of Geosciences, Beijing 100083, China.

E-mail address: dmliu@cugb.edu.cn (D. Liu), Tel: +86-10-82323971; fax: + 86-10-82326850.

Abstract

Pore system in coal is highly heterogeneous, while it is the main occurrence space and transport channel for coalbed methane (CBM). Electric pulse fracturing (EPF) has been considered as an effective approach to improve the coal physical properties for better CBM production. In this work, based on AFM measurement of 40 coal samples collected from Qinshui Basin, we evaluated the physical properties of coal, adsorbed with different cations, after EPF. This was accomplished by first analyzing the breakdown field response process of coal adsorbed with different cations, and then determining the dynamic changes of pore and surface roughness using the watershed